

# Nitrogen as a Tracer of Giant Planet Formation. I.: A Universal Deep Adiabatic Profile and Semi-analytical Predictions of Disequilibrium Ammonia Abundances in Warm Exoplanetary Atmospheres

KAZUMASA OHNO<sup>1</sup> AND JONATHAN J. FORTNEY<sup>1</sup>

<sup>1</sup>*Department of Astronomy & Astrophysics, University of California, Santa Cruz, 1156 High St, Santa Cruz, CA 95064, USA*

## ABSTRACT

A major motivation of spectroscopic observations of giant exoplanets is to unveil planet formation processes from atmospheric compositions. Several recent studies suggested that atmospheric nitrogen, like carbon and oxygen, can provide important constraints on planetary formation environments. Since nitrogen chemistry can be far from thermochemical equilibrium in warm atmospheres, we extensively investigate under what conditions, and with what assumptions, the observable NH<sub>3</sub> abundances can diagnose an atmosphere’s bulk nitrogen abundance. In the first paper of this series, we investigate atmospheric T-P profiles across equilibrium temperature, surface gravity, intrinsic temperature, atmospheric metallicity, and C/O ratio using a 1D radiative-convective equilibrium model. Models with the same intrinsic temperature and surface gravity coincide with a shared “universal” adiabat in the deep atmosphere, across a wide equilibrium temperature range (250-1200 K), which is not seen in hotter or cooler models. We explain this behavior in terms of the classic “radiative zero solution” and then establish a semi-analytical T-P profile of the deep atmospheres of warm exoplanets. This profile is then used to predict vertically quenched NH<sub>3</sub> abundances. At solar metallicity, our results show that the quenched NH<sub>3</sub> abundance only coincides with the bulk nitrogen abundance (within 10%) at low intrinsic temperature, corresponding to a planet with a sub-Jupiter mass ( $\lesssim 1 M_J$ ) and old age ( $\gtrsim 1$  Gyr). If a planet has a high metallicity ( $\gtrsim 10\times$  solar) atmosphere, the quenched NH<sub>3</sub> abundance significantly underestimates the bulk nitrogen abundance at almost all planetary masses and ages. We suggest modeling and observational strategies to improve the assessment of bulk nitrogen from NH<sub>3</sub>.

## 1. INTRODUCTION

Planetary atmospheric compositions offer valuable clues to the planet formation and evolution process, especially for giant planets with primordial atmospheres. Over the past decade a number of studies have suggested that atmospheric elemental ratios, such as the carbon-to-oxygen ratio (C/O), can diagnose the orbital distance where a planet initially forms (e.g., Öberg et al. 2011; Madhusudhan et al. 2014, 2017; Ali-Dib et al. 2014; Helling et al. 2014; Thiabaud et al. 2015; Piso et al. 2015, 2016; Öberg & Bergin 2016; Cridland et al. 2016, 2017, 2019; Espinoza et al. 2017; Eistrup et al. 2016, 2018, 2022; Booth et al. 2017; Booth & Ilee 2019; Öberg & Wordsworth 2019; Ohno & Ueda 2021; Turrini et al. 2021; Schneider & Bitsch 2021a; Mollière et al. 2022; Pacetti et al. 2022; Bitsch et al. 2022; Notsu et al. 2022; Eistrup 2022). Many previous studies focused on the atmospheric C/O ratio, as it has significant impacts on atmospheric chemistry and likely leaves observable fingerprints (e.g., Madhusudhan 2012; Moses et al. 2013a,b; Mollière et al. 2015; Drummond et al. 2019; Notsu et al. 2020; Dash et al. 2022). Beyond the C/O ratio, several recent studies also have also discussed the potential importance of other elements, such as nitrogen (Piso et al. 2016; Cridland et al. 2020; Ohno & Ueda 2021; Notsu et al. 2022), sulfur (Tur-

rini et al. 2021; Pacetti et al. 2022), and refractory metals (Lothringer et al. 2021; Schneider & Bitsch 2021b; Hands & Helled 2022; Chachan et al. 2022).

Nitrogen is the third most abundant volatile element in solar composition and may provide important constraints on the planetary formation environments. Nitrogen has particular advantages to probe the formation locations. Piso et al. (2016) first pointed out that the N/O ratio of disk gas is always higher than stellar N/O by a factor of  $\geq 2$  and monotonically increases with radial distance, which provides additional clues to constrain planetary formation location from a planet’s atmospheric N/O ratio. Cridland et al. (2020) studied the atmospheric compositions of warm Jupiters using a population synthesis model and suggested that combining C/O and N/O helps to probe the formation history, such as whether the planet acquired its atmosphere outside of the refractory carbon erosion front. Ohno & Ueda (2021) also stressed that the atmospheric N/O is expected to be sensitive to formation location if disk solids, such as pebbles and planetesimals, determine the atmospheric composition. This is because the solid N/O ratio has an order-of-magnitude variation as a function of a radial distance (see also Notsu et al. 2022 for the discussion based on a disk chemistry model). Turrini et al. (2021) and Pacetti et al. (2022) suggested that

C/N, N/O, and S/N ratios help to constrain the formation and migration pathways of giant planets.

To clarify the usefulness of the N/O ratio for example, Figure 1 shows the nitrogen-to-oxygen ratio (N/O) of solids and gas in a protoplanetary disk computed by the phase equilibrium model of Ohno & Ueda (2021) for the protosolar disk model of Öberg & Wordsworth (2019). The gas-phase N/O monotonically increases with orbital distance, as the O-bearing molecules (e.g.,  $\text{H}_2\text{O}$ ,  $\text{CO}_2$ ) are gradually removed from gas phase via condensation while most of N remains as a highly volatile  $\text{N}_2$  gas within  $\text{N}_2$  snowline. The solid-phase N/O shows an order-of-magnitude orbital variation because of large abundance difference between  $\text{NH}_3$  and  $\text{N}_2$  (e.g., Öberg & Bergin 2021). The latter indicates the strong dependence of atmospheric N/O to formation location if solid (e.g., planetesimal) accretion predominantly determines the atmospheric composition.

It is also worth noting that several recent studies have discussed formation scenarios for Jupiter in our solar system. Motivated by the nitrogen abundance being comparable to other heavy elements in the Jovian atmosphere (for recent review, see Guillot et al. 2022; Atreya et al. 2022), Öberg & Wordsworth (2019) and Bosman et al. (2019) proposed that Jupiter might have initially formed outward of the  $\text{N}_2$  snowline beyond 30 AU where solid elemental ratios coincide with solar values (see also Owen et al. 1999). Ohno & Ueda (2021) suggested that the Jovian atmospheric composition could also be explained if Jupiter formed at a locally cold disk region caused by the shadow cast by a disk substructure, such as a dust pileup at  $\text{H}_2\text{O}$  snowline, which is not nearly at far away from the central star.

In substellar atmospheres, in the absence of ionizing flux,  $\text{N}_2$  and  $\text{NH}_3$ , are the main nitrogen reservoirs (Lodders & Fegley 2002). HCN can also be abundant if photochemical processes are at work (Moses et al. 2013a).  $\text{NH}_3$  and HCN would be likely detectable by near future infrared observations by JWST and Ariel (MacDonald & Madhusudhan 2017), while  $\text{N}_2$  is in general not observable due to the negligibly low visible and infrared opacity for the temperature regime of exoplanets. Hobbs et al. (2019) used a photochemical kinetic model to show that the abundances of C- and O-bearing species, such as  $\text{H}_2\text{O}$  and  $\text{CO}$ , are insensitive to N/H ratio in hot Jupiters like HD 209458b. Ramírez et al. (2020) also investigated the impact of N/H ratio on TiO abundances in ultra-hot Jupiters and found that the TiO abundance is nearly independent of N/H. Since C- and O-bearing species abundances are insensitive to bulk nitrogen abundance in sub-stellar atmospheres, it appears that the only route to diagnose the bulk nitrogen abundance of a giant planet is from  $\text{NH}_3$  and/or HCN.

However, constraining the bulk nitrogen abundance from  $\text{NH}_3$  and HCN is a complex task. The  $\text{NH}_3$  and HCN abun-

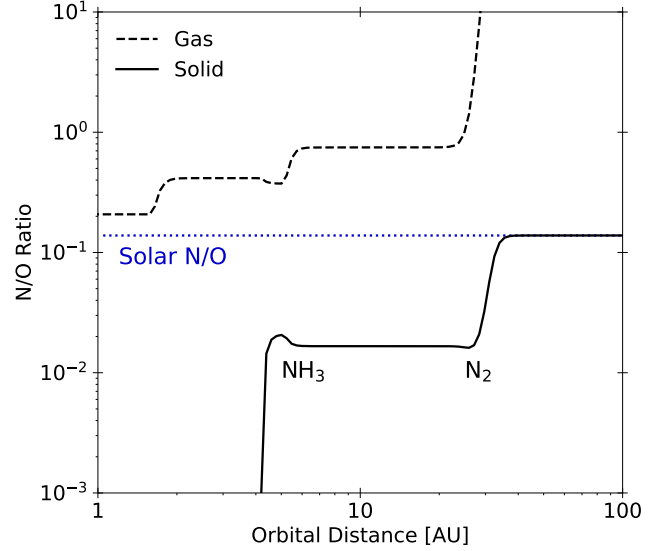


**Figure 1.** The nitrogen-to-oxygen ratio as a function of orbital distance in a protoplanetary disk model. The black dashed and solid lines show the N/O ratio of disk gas, and solids, respectively. The solar ratio is shown in dotted blue. We compute this profile using the phase equilibrium model of Ohno & Ueda (2021) assuming the disk model of Öberg & Wordsworth (2019).

dances in the observable atmosphere readily deviates from thermochemical equilibrium abundances because of disequilibrium effects, such as vertical mixing and photochemistry (e.g., Moses et al. 2011; Line et al. 2011; Venot et al. 2013). For warm planets of  $T_{\text{eq}} \lesssim 1000$  K, Fortney et al. (2020) investigated disequilibrium  $\text{NH}_3$  abundances on Saturn-like planets with various  $T_{\text{eq}}$  and found that  $\text{NH}_3$  abundance depends on a number of factors, such as planetary mass, age, and metallicity. They also suggested that  $\text{N}_2$  will actually dominate over  $\text{NH}_3$  over a very wide range of temperature and ages, making the observable  $\text{NH}_3$  abundance only a lower limit of bulk nitrogen abundance. Hu (2021) also investigated photochemistry on temperate/cold  $\text{H}_2$ -rich planets and found that  $\text{NH}_3$  tends to be depleted due to photodissociation, especially on planets around G/K stars.

In this study, we expand the work of Fortney et al. (2020) with a particular focus on nitrogen chemistry. Here in Paper I we systematically investigate the thermal structure of planetary deep atmosphere, which significantly affects the disequilibrium abundance of  $\text{NH}_3$ , as demonstrated by Fortney et al. (2020). While Fortney et al. (2020) investigated the effects of planetary deep atmospheres using numerical models, this study advances the field by establishing a semi-analytical model that explicitly links planetary gravity, intrinsic temperature, metallicity, bulk nitrogen abundance, and disequilibrium  $\text{NH}_3$  abundance. The model is readily applicable to arbitrarily planets and will be useful to interpret the retrieved  $\text{NH}_3$  abundance in future observations.

The organization of this paper is as follows. In Section 2, we introduce a basic background of nitrogen equilibrium and disequilibrium chemistry. In Section 3, we investigate atmospheric pressure-temperature ( $P$ - $T$ ) profiles for a wide range of planetary parameters. We derive a semi-analytical fit to understand why giant planets typically have a universal deep adiabat, irrespective of incident flux, which has a major impact on  $\text{NH}_3$  abundances from disequilibrium chemistry from vertical mixing. In Section 4, we identify the relation between  $\text{NH}_3$  and bulk nitrogen abundances as a function of planetary parameters from semi-analytical arguments. In Section 5, we describe caveats of this study. In Section 6, we summarize our findings. In the paper II of this series (Ohno & Fortney 2022), we verify our semi-analytical predictions using a photochemical kinetics model and discuss the observational implications for atmospheric nitrogen species on transmission and emission spectra.

## 2. NITROGEN CHEMISTRY: THE IMPORTANCE OF THE DEEP ATMOSPHERE STRUCTURE

One of the important factors in controlling the observable  $\text{NH}_3$  abundance is vertical vertical mixing within an atmosphere. Atmospheric compositions follow thermochemical equilibrium in the deep hot atmospheres, while the abundances at lower pressure, where it is colder, tend to be out of equilibrium, vertically constant, and reflect the equilibrium compositions of the deep atmosphere (though see Section 5.2 for a caveat on this picture). This phenomena is often called “quenching” (e.g., Fegley & Prinn 1985; Fegley & Lodders 1994; Zahnle & Marley 2014; Tsai et al. 2018) and was originally identified for  $\text{CO}/\text{CH}_4$  in the Jovian atmosphere, where detected  $\text{CO}$  abundances are many orders of magnitude higher than thermochemical equilibrium calculations (Prinn & Barshay 1977). This quenching is caused by the slow thermochemical conversion, compared to relatively fast vertical mixing (e.g., Moses et al. 2011). Several recent studies have attempted to constrain the strength of vertical mixing in brown dwarf and giant planet atmospheres from quenched molecular abundances (Miles et al. 2020; Kawashima & Min 2021; Mukherjee et al. 2022b).

Since the upper atmospheric composition is related to the composition of deep hot atmosphere, it is necessary to understand the planetary deep atmosphere and interior to relate the observable  $\text{NH}_3$  abundance with bulk nitrogen abundance (Fortney et al. 2020). To this end, we first introduce the nitrogen chemistry in deep atmospheres where thermochemical equilibrium is expected.

### 2.1. Thermochemical equilibrium and vertical quenching of $\text{NH}_3$

The quenching behavior of  $\text{NH}_3$  has an interesting characteristic: the quenched  $\text{NH}_3$  abundance is insensitive to the

strength of vertical mixing (Saumon et al. 2006; Zahnle & Marley 2014; Fortney et al. 2020). As discussed in Zahnle & Marley (2014), this is caused by the abundance ratio contours of  $\text{NH}_3/\text{N}_2$  being nearly parallel to the adiabatic profiles of substellar atmospheres (see also Figure 2). The vertically quenched abundance is determined, to a good approximation, by the equilibrium abundance at certain depth where thermochemical interconversion timescale becomes equal to the vertical mixing timescale. However, since the deep adiabat is nearly along the contour of constant  $\text{NH}_3/\text{N}_2$  ratio, the quenched  $\text{NH}_3$  abundance is nearly the same wherever the quenching takes place. This characteristic has an advantage in interpreting the quenched  $\text{NH}_3$ : one does not need to worry too much about the uncertainty of vertical mixing strength, parameterized by  $K_{zz}$ .

To further clarify the quenching behavior of  $\text{NH}_3$ , the right panel of Figure 2 shows the vertical distribution of  $\text{NH}_3$  in a solar composition atmosphere computed by the chemical kinetics code VULCAN (Tsai et al. 2017, 2021) for various planetary equilibrium temperature and eddy diffusion coefficients. While the  $\text{NH}_3$  distribution in the upper atmosphere depends on the eddy diffusion coefficient for hot ( $T_{\text{eq}} \gtrsim 1000$  K) planets where the quenching occurs at shallower radiative parts of the atmosphere, the abundances are nearly independent of the eddy diffusion at warm ( $T_{\text{eq}} < 1000$  K) planets where the quenching occurs at deep adiabatic atmospheres.

Since the quenched abundance is determined by the composition of a deep atmosphere point where thermochemical equilibrium is valid, it is worth first examining the equilibrium abundance of nitrogen species. The law of mass action provides the relation of  $\text{N}_2$  and  $\text{NH}_3$  that should be satisfied in thermochemical equilibrium, given by

$$\frac{P_{\text{NH}_3}^2}{P_{\text{N}_2} P_{\text{H}_2}^3} = K_{\text{N}_2 \rightleftharpoons \text{NH}_3} = A e^{B/T}, \quad (1)$$

where  $P_{\text{H}_2}$ ,  $P_{\text{N}_2}$ , and  $P_{\text{NH}_3}$  are the partial pressure of  $\text{H}_2$ ,  $\text{N}_2$ , and  $\text{NH}_3$ , respectively,  $K_{\text{N}_2 \rightleftharpoons \text{NH}_3}$  is the equilibrium constant of  $\text{N}_2$ - $\text{NH}_3$  interconversion ( $\text{N}_2 + 3\text{H}_2 \rightleftharpoons 2\text{NH}_3$ ),  $A = 5.90 \times 10^{-13} \text{ bar}^{-2}$ , and  $B = 13207 \text{ K}$  (Zahnle & Marley 2014). Assuming that  $\text{N}_2$  and  $\text{NH}_3$  accommodate most of the nitrogen, we can approximate the nitrogen conservation as  $f_{\text{N}} \approx f_{\text{NH}_3} + 2f_{\text{N}_2}$ , where  $f_{\text{N}}$ ,  $f_{\text{N}_2}$ , and  $f_{\text{NH}_3}$  are volume mixing ratios of total nitrogen,  $\text{N}_2$ , and  $\text{NH}_3$ . Then, one can obtain the pressure-temperature relation of  $\text{NH}_3/\text{N}_2 = \xi$  contour as (Zahnle & Marley 2014)

$$f_{\text{N}} \left( \frac{\xi^2}{2 + \xi} \right) = P^2 f_{\text{H}_2}^3 A e^{B/T}, \quad (2)$$

where  $f_{\text{H}_2} = \text{H}_2/(\text{H}_2 + \text{He}) = 0.859$  and  $f_{\text{N}} = 1.16 \times 10^{-4}$  in solar elemental abundances of Asplund et al. (2021). We

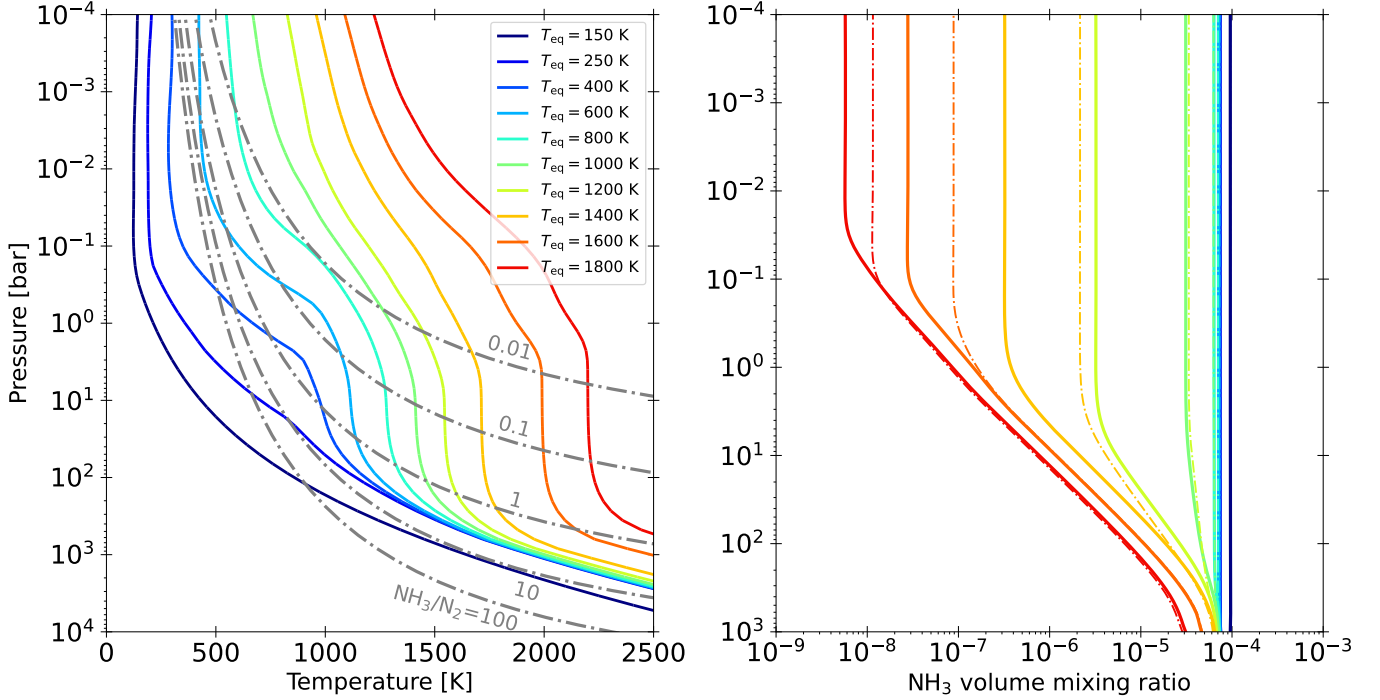


**Figure 2.** (Left)  $P$ - $T$  profiles of solar composition atmospheres computed in radiative-convective equilibrium (see Section 3.2 for details). Different colored lines show the  $P$ - $T$  profiles for different equilibrium temperatures. We assume a surface gravity of  $g = 10 \text{ m s}^{-2}$  and planetary intrinsic temperature of  $T_{\text{int}} = 100 \text{ K}$ . The gray dashed lines show the abundance ratio contours of  $\text{NH}_3/\text{N}_2 = 0.01, 0.1, 1, 10, 100$  from top to bottom, computed by Equation (2). (Right) Vertical distribution of  $\text{NH}_3$  volume mixing ratio for the  $P$ - $T$  profiles in the left panel. The solid and dash-dot lines show the distributions for eddy diffusion coefficients of  $10^8$  and  $10^{10} \text{ cm}^2 \text{ s}^{-1}$ , respectively. Note that the distributions of different eddy diffusion coefficients are almost superimposed on each other at  $T_{\text{eq}} < 1000 \text{ K}$ . We have turned off photochemistry for the sake of simplicity.

note that  $f_{\text{N}}$  is not identical to the  $\text{N}/\text{H}$  ratio, as it is given by

$$f_{\text{N}} = \frac{\text{N}}{\text{H}_2 + \text{He}} = \frac{2\text{N}/\text{H}}{1 + 2\text{He}/\text{H}} = 2f_{\text{H}_2}\text{N}/\text{H}, \quad (3)$$

where  $\text{N}/\text{H} = 6.76 \times 10^{-5}$  is the value for solar composition (Asplund et al. 2021). Equation (2) is inconvenient from an observational perspective, as both  $f_{\text{N}}$  and  $\xi$  are unknown. Instead, eliminating  $f_{\text{N}_2}$  in Equation (1) using  $f_{\text{N}} \approx f_{\text{NH}_3} + 2f_{\text{N}_2}$ , we obtain

$$\text{N}/\text{H} = \frac{f_{\text{NH}_3}}{2f_{\text{H}_2}} \left[ 1 + \frac{2f_{\text{NH}_3}e^{-B/T}}{Af_{\text{H}_2}^3P^2} \right], \quad (4)$$

where we use Equation (3). Under chemical equilibrium, Equation (4) can straightforwardly constrain the bulk nitrogen abundance from the  $\text{NH}_3$  abundance. In addition, as introduced above, the equilibrium  $\text{NH}_3$  abundance is approximately constant along the deep adiabatic profiles. Thus, it is expected that the quenched  $\text{NH}_3$  abundance is mostly determined by the deep adiabatic profile alone.

### 3. CONSTRAINING THERMAL STRUCTURES OF DEEP ATMOSPHERES

#### 3.1. Radiative Zero Solution of Irradiated Exoplanets

The preceding argument highlights the importance of identifying the thermal structures of deep atmospheres (below the photosphere) to relate the quenched  $\text{NH}_3$  abundance with bulk nitrogen abundance. Here, we point out an interesting trend of deep atmospheres: many planets with different equilibrium temperatures<sup>1</sup> ( $T_{\text{eq}} = 250$ – $1200 \text{ K}$ ) have nearly the same deep adiabatic profile as seen in Figure 2. Fortney et al. (2007) first reported such a universal deep adiabat in their radiative-convective models. Motivated by simplified calculations with dual-band radiative transfer (Guillot 2010), Fortney et al. (2020) speculated that the universal deep adiabat may emerge owing to the steep change of visible-to-infrared opacity ratio caused by the loss of gas-phase alkali metals, although the actual cause still remains unclear. The universality of the deep adiabat has a crucial impact on the disequilibrium abundance of  $\text{NH}_3$ : the quenched  $\text{NH}_3$  abundance is nearly independent of the equilibrium temperature for temperate to warm exoplanets, as seen in the right panel of Figure 2.

<sup>1</sup> We refer the equilibrium temperature to the temperature for zero Bond albedo with full heat redistribution unless otherwise indicated.



Here, we elaborate why many planets have nearly the same deep adiabatic profile for a wide range of equilibrium temperatures. The common thermal structure independent of upper boundary conditions is reminiscent of the “radiative zero solution” discussed in the context of stellar and protoplanetary envelope structures (e.g., Hayashi et al. 1962; Mizuno 1980; Stevenson 1982; Kippenhahn & Weigert 1994). In purely radiative atmospheres without convection, the atmospheric temperature structure follows

$$\left(\frac{d \ln T}{d \ln P}\right)_{\text{rad}} = \frac{3\kappa L_{\text{int}}}{64\pi\sigma GM} \frac{P}{T^4} = \frac{3\kappa_0 P^{1+\alpha} T^\beta}{16g} \frac{T_{\text{int}}^4}{T^4}, \quad (5)$$

where  $L_{\text{int}} = 4\pi R^2 \sigma T_{\text{int}}^4$  is the planetary intrinsic luminosity,  $T_{\text{int}}$  is the planetary intrinsic temperature,  $\sigma$  is the Stefan-Boltzmann constant,  $g = GM/R^2$  is the planetary gravity, and  $\kappa = \kappa_0 P^\alpha T^\beta$  is the atmospheric Rosseland-mean opacity. Assuming constant gravity,  $\alpha$ , and  $\beta$ , Equation (5) yields an analytical solution of

$$T = T_0 + \left[ \frac{3\kappa_0 T_{\text{int}}^4 (4 - \beta)}{16g(1 + \alpha)} \right]^{1/(4-\beta)} (P^{(1+\alpha)/(4-\beta)} - P_0^{(1+\alpha)/(4-\beta)}), \quad (6)$$

where  $P_0$  and  $T_0$  are the pressure and temperature of the upper boundary. For  $(4 - \beta)/(1 + \alpha) > 0$ <sup>2</sup>, since  $P \gg P_0$  and  $T \gg T_0$  in the limit of a deep atmosphere, the temperature structure asymptotically approaches the same temperature structure relation with  $P_0 = 0$  and  $T_0 = 0$  in Equation (6) regardless of the upper boundary condition, which is called the radiative-zero solution (e.g., Hayashi et al. 1962; Mizuno 1980; Stevenson 1982; Kippenhahn & Weigert 1994).

The radiative zero solution does not necessarily apply for atmospheric structures, as convection sets in to force the temperature gradient to the adiabatic temperature gradient  $\nabla_{\text{ad}}$ . In the convective region, from the definition of the adiabatic gradient  $(d \ln T / d \ln P) = \nabla_{\text{ad}}$ , the temperature structure follows

$$T = T_{\text{rcb}} \left( \frac{P}{P_{\text{rcb}}} \right)^{\nabla_{\text{ad}}}, \quad (8)$$

where  $P_{\text{rcb}}$  and  $T_{\text{rcb}}$  are pressure and temperature of radiative-convective boundary (RCB), and we assume a constant adiabatic gradient for the sake of simplicity. Inserting Equation (6) into this equation with  $P = P_{\text{rcb}} \gg P_0$ , the deep adiabatic

<sup>2</sup> For  $(4 - \beta)/(1 + \alpha) < 0$ , the temperature structure converges to the following isothermal profile in the limit of  $P \gg P_0$ :

$$T \approx T_0 - \left[ \frac{3\kappa_0 T_{\text{int}}^4 P_0^{1+\alpha} (4 - \beta)}{16g(1 + \alpha)} \right]^{1/(4-\beta)}. \quad (7)$$

In this case, the upper boundary conditions controls the temperature structure of the deep atmosphere.

temperature can be expressed by

$$T = \left[ T_0 + \left( \frac{3\kappa_0 T_{\text{int}}^4 P_{\text{rcb}}^{1+\alpha} (4 - \beta)}{16g(1 + \alpha)} \right)^{1/(4-\beta)} \right] \left( \frac{P}{P_{\text{rcb}}} \right)^{\nabla_{\text{ad}}}, \quad (9)$$

This equation could strongly depend on the upper boundary condition if the first term in the prefactor (i.e.,  $T_0$ ) dominates over the second term. In other words, the deep adiabatic profile does depend on the upper boundary condition if the atmospheric  $P$ - $T$  profile meets the RCB before it converges to the radiative-zero solution.

Based on the preceding argument, we suggest that planets have the common deep adiabatic profile regardless of stellar insolation if the  $P$ - $T$  profile converges to the radiative zero solution above the RCB pressure level. Equating Equation (5) and  $\nabla_{\text{ad}}$ , the RCB pressure is given by

$$P_{\text{rcb}} = \left( \frac{16g T_{\text{rcb}}^{4-\beta}}{3\kappa_0 T_{\text{int}}^4 \nabla_{\text{ad}}} \right)^{1/(1+\alpha)}. \quad (10)$$

Inserting Equation (10) into (6), we obtain the relation between the RCB temperature and upper boundary temperature  $T_0$  as

$$\frac{T_0}{T_{\text{rcb}}} \approx 1 - \phi^{1/(4-\beta)}, \quad (11)$$

where we have approximated  $P_0 = 0$ , as  $P_{\text{rcb}} \gg P_0$ . We have introduced a dimensionless parameter defined as

$$\phi \equiv \frac{4 - \beta}{1 + \alpha} \nabla_{\text{ad}}. \quad (12)$$

The  $\phi$  parameter is equivalent to the ratio of adiabatic temperature gradient to the radiative temperature gradient in the limit of deep atmospheres. Equation (11) is invalid at  $\phi > 1$  because one cannot define an RCB in the atmosphere with  $\phi > 1$ , where convection does not occur (see Appendix 1). Meanwhile, solving the equality of the first and second terms in the prefactor of Equation (9) with respect to  $P_{\text{rcb}}$ , we can evaluate a threshold RCB pressure above which the thermal structure converges to the radiative zero solution before it meets the RCB, as

$$P_{\text{thr}} = \left[ \frac{16g T_0^{4-\beta} (1 + \alpha)}{3\kappa_0 T_{\text{int}}^4 (4 - \beta)} \right]^{1/(1+\alpha)}. \quad (13)$$

Taking the ratio of Equation (10) to (13) with (11), we achieve the diagnostic metric, given by

$$\begin{aligned} \frac{P_{\text{rcb}}}{P_{\text{thr}}} &= \left( \frac{4 - \beta}{1 + \alpha} \nabla_{\text{ad}} \right)^{1/(1+\alpha)} \left( \frac{T_{\text{rcb}}}{T_0} \right)^{(4-\beta)/(1+\alpha)} \\ &= [\phi^{1/(\beta-4)} - 1]^{(\beta-4)/(\alpha+1)} \end{aligned} \quad (14)$$

If  $P_{\text{rcb}}/P_{\text{thr}} > 1$ , the  $P$ - $T$  profile converges to the radiative zero solution before it meets the RCB, resulting in a deep

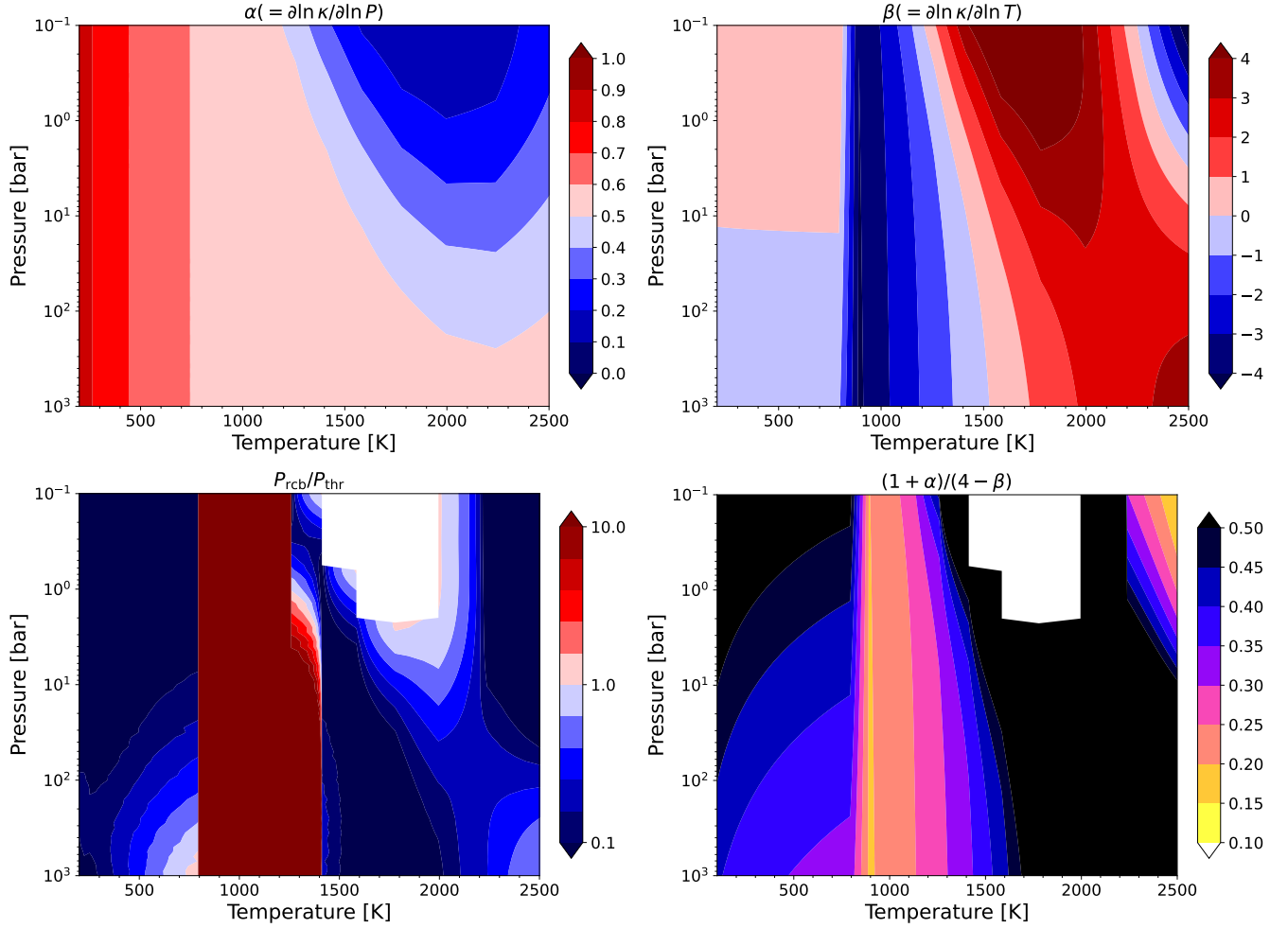


**Figure 3.** (Upper left and right panels) Pressure and temperature dependence of the Rosseland mean opacity of a solar composition gas, based on the [Freedman et al. \(2014\)](#) analytic opacity fit. (Lower left) The ratio of the RCB pressure to the threshold RCB pressure estimated by Equation (14). The  $P$ - $T$  profile converges to the radiative zero solution before it meets the RCB for  $P_{\text{rcb}}/P_{\text{thr}} > 1$  (redder colors), leading to the deep adiabatic profile that is insensitive to stellar insolation. The black contour denotes  $P_{\text{rcb}}/P_{\text{thr}} = 1$ . (Lower right) The pressure dependence of the radiative zero solution,  $(1 + \alpha)/(4 - \beta)$ . It is expected that the  $P$ - $T$  profiles tend to converge to the same radiative zero solution of  $T \propto P^{(1+\alpha)/(4-\beta)}$  in the  $P$ - $T$  space with the same value of  $(1 + \alpha)/(4 - \beta)$ . We have filled the space of  $(1 + \alpha)/(4 - \beta) < 0$  in white for clarity. In computing the bottom left panel, we set  $\phi = 1$  when  $\phi$  exceeds unity, as the  $P$ - $T$  profile always converges to the radiative-zero solution at  $\phi \geq 1$ .

adiabatic profile being independent of upper boundary condition, i.e., level of stellar insolation. Interestingly, Equation (14) indicates that whether or not stellar insolation affects the deep profile only depends on the adiabatic gradient and atmospheric opacity law.

Next we investigate Equation (14) using the opacity of solar composition gas, from [Freedman et al. \(2014\)](#). We numerically compute  $\alpha$  and  $\beta$  from the analytical fit of the Rosseland-mean opacity obtained by [Freedman et al. \(2014\)](#) as a function of pressure and temperature, as shown in the upper two panels of Figure 3. While previous studies adopted single values of  $\alpha$  and  $\beta$  (e.g., [Rogers & Seager 2010](#); [Owen & Wu 2017](#); [Ginzburg et al. 2018](#)), these values differ at different pressure and temperature conditions. We also note that since the complex [Freedman et al. \(2014\)](#) analytic fitting for-

mula changes at 800 K, which is necessary since the opacities change with  $T$ , this leads to plots of  $\beta$  that somewhat exaggerate the sharpness of this change to the opacities. The adiabatic gradient is taken from the equation of state (EOS) for H/He mixtures ([Chabrier et al. 2019](#)), which has updated the widely used SCvH EOS ([Saumon et al. 1995](#)). The lower left panel of Figure 3 shows  $P_{\text{rcb}}/P_{\text{thr}}$  as a function of pressure and temperature. We find that the RCB pressure is much higher than the threshold pressure in the temperature range of  $\sim 800$ – $1400$  K. Actually, the  $\phi$  parameter takes a value of  $\phi \gtrsim 1$  in that temperature range, which prohibits the transition from radiative to convective atmospheres. This indicates that the  $P$ - $T$  profiles tend to converge to the radiative zero solution before reaching the RCB in that temperature range. In Figure 2,  $P$ - $T$  profiles indeed converge to the same deep

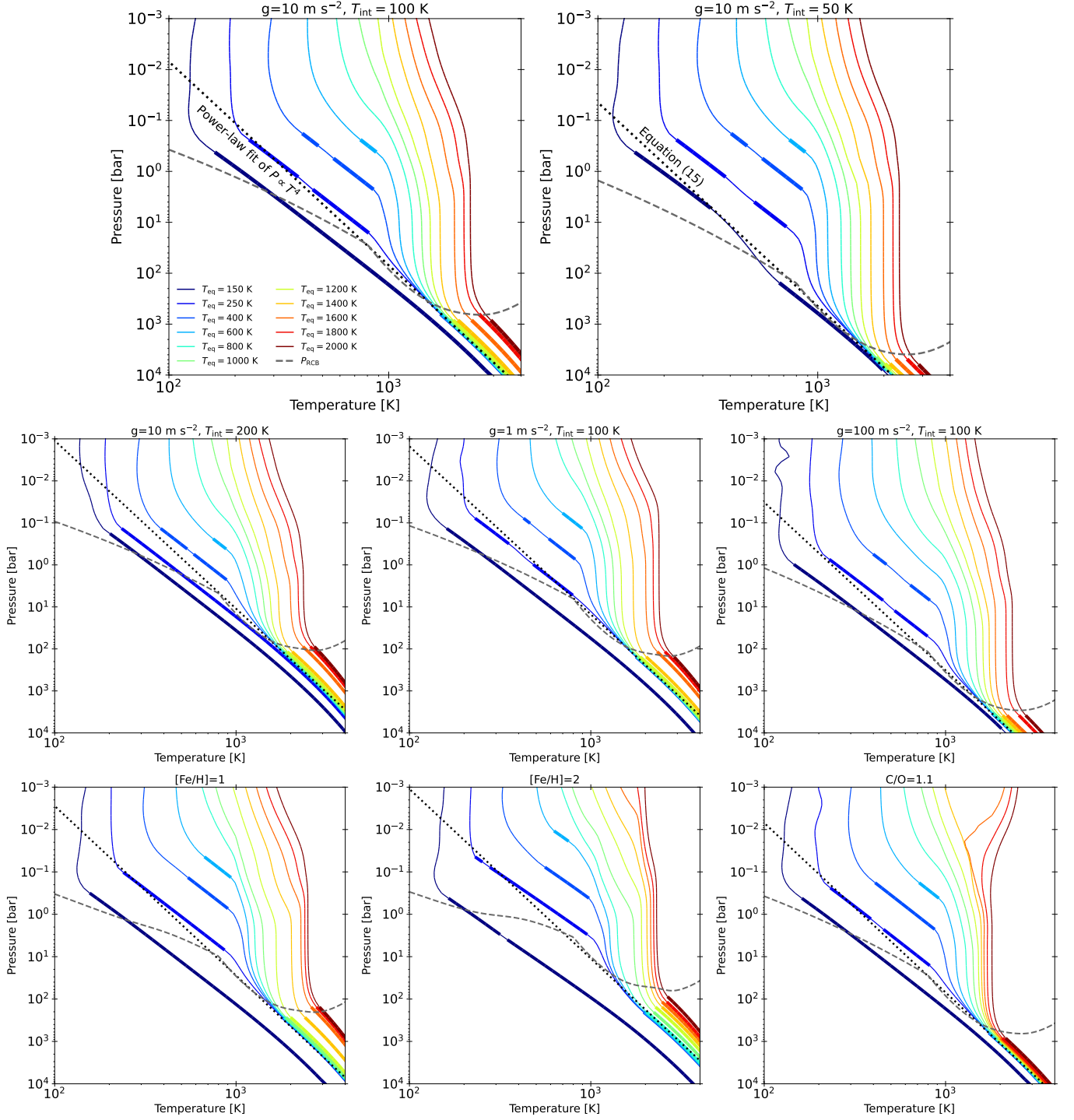


**Figure 4.**  $P$ - $T$  profiles for a variety of planetary surface gravities, intrinsic temperatures, atmospheric metallicities, and C/O ratios. All models are 1D radiative-convective equilibrium. The thicker lines denote convective regions, and thin lines show the radiative regions. The gray dashed line plots the RCB pressure estimated from Equation (10) with the Rosseland mean opacity of [Freedman et al. \(2014\)](#), which reasonably explains the deep innermost RCB found in numerical results. The black dotted line shows our semi-analytical fit of the deep adiabatic  $P$ - $T$  profile (Equation 15), which the  $P$ - $T$  profiles converge on, for  $T_{\text{eq}} \sim 250$ –1200 K.

adiabatic profile when the temperature at the second (deeper) nearly isothermal region at  $P \sim 10\text{--}100$  bar falls into  $\sim 800\text{--}1500$  K, consistent with the phase space of  $P_{\text{rcb}}/P_{\text{thr}} \gg 1$  in Figure 3. Fortney et al. (2007) and Fortney et al. (2020) also obtained the  $P\text{--}T$  profiles converging to same deep adiabatic line when the same condition applies.

We note that the deep adiabatic profile might diverge even if the  $P\text{--}T$  profile converges to the radiative zero solution. This is because the temperature structure obeys  $T \propto P^{(1+\alpha)/(4-\beta)}$  in the radiative zero solution (Equation 6), where different power-law index of  $(1+\alpha)/(4-\beta)$  yields different temperature structure lines. As shown in the bottom right panel of Figure 3, the index is roughly constant,  $(1+\alpha)/(4-\beta) \sim 0.25$ , in the temperature range of  $\sim 800\text{--}1300$  K. Thus, it might be expected that the  $P\text{--}T$  profiles tend to converge to the radiative-zero solution of  $T \propto P^{0.25}$  in this temperature range where Equation (14) predicts  $P_{\text{rcb}} \gtrsim P_{\text{thr}}$ .

### 3.2. Numerical Exploration of $P\text{--}T$ profiles

To further study the thermal structure of deep atmospheres, we explore the PT profiles at wide range of planetary properties using EGP, a version of the 1D radiative-convective equilibrium model of McKay et al. (1989) and Marley & McKay (1999)<sup>3</sup>. The model solves for radiative-convective equilibrium in a plane-parallel atmosphere based on the algorithm of Toon et al. (1989) with thermochemical equilibrium accounting for rain-out effects (Fegley & Lodders 1994; Lodders & Fegley 2002; Visscher et al. 2006, 2010). The model implements non-gray atmospheric opacity with the correlated-k approximation, where we adopt correlated k-coefficients datasets calculated for 1060 pressure-temperature grid points (Lupu et al. 2021, see references therein for the details of opacity sources). We note that our calculations omit TiO/VO opacity, except for the C/O = 1.1 models. In convective layers, the model switches to use the adiabatic temperature gradient extracted from the equation of state for H/He mixture with  $Y = 0.292$  in Chabrier et al. (2019). The model has been extensively applied for solar system objects (McKay et al. 1989; Marley & McKay 1999; Fortney et al. 2011), exoplanets (Fortney et al. 2005, 2007, 2008, 2020; Morley et al. 2013, 2015, 2017; Thorngren et al. 2019; Gao et al. 2020; Mayorga et al. 2021), and brown dwarfs (Marley et al. 1996, 2021; Saumon & Marley 2008; Morley et al. 2012, 2014; Robinson & Marley 2014; Tang et al. 2021; Karalidi et al. 2021; Mukherjee et al. 2022b). We refer readers to Marley & Robinson (2015) and Marley et al. (2021) for further details of the radiative-convective equilibrium model.

Figure 4 shows  $P\text{--}T$  profiles for various values of the planetary equilibrium temperature, surface gravity, intrinsic tem-

perature, atmospheric metallicity, and C/O ratio. As found in previous studies, cooler planets ( $T_{\text{eq}} \lesssim 1000$  K) tend to have steeper temperature gradients, which yields hotter middle atmospheres ( $P \sim 0.1\text{--}1$  bar) as compared to the equilibrium temperature. The cooler atmospheres ( $T_{\text{eq}} \lesssim 250\text{--}600$  K) also develop detached convective layers at around  $P \sim 0.1\text{--}10$  bar. A convective zone at these pressures is found in non-irradiated models at these  $T_{\text{eff}}$  values, and is the “natural” outcome for these atmospheres, given the high thermal infrared opacities (Marley & Robinson 2015). Such convective zones are not possible in the more highly irradiated objects given the high temperatures at low pressure, which forces a shallower-than-adiabatic temperature gradient throughout much of the atmosphere.

The  $P\text{--}T$  profiles converge to the same deep adiabatic profile in the equilibrium temperature range of  $T_{\text{eq}} \sim 250\text{--}1200$  K for a given set of planetary intrinsic temperature, gravity, and atmospheric compositions. For solar metallicity with  $g = 1, 10$ , and  $100 \text{ m}^2 \text{ s}^{-1}$  and  $T_{\text{int}} = 50, 100$ , and  $200$  K (top five panels), planets with the equilibrium temperature of  $T_{\text{eq}} = 250\text{--}1200$  K have nearly the same  $P\text{--}T$  profiles in deep convective layers. These atmospheric models have temperatures in the middle atmosphere ( $P \sim 10\text{--}100$  bar) between  $\sim 1000\text{--}1500$  K, which is consistent with the criterion argued in the previous section.  $P\text{--}T$  profiles also tend to converge to the same adiabatic profile for high metallicity models of  $[\text{Fe}/\text{H}] = +1$  and  $+2$ , as well as a higher C/O model of C/O = 1.1. At very high metallicities, the deep adiabatic profiles starts to deviate from the same deep profile at a lower equilibrium temperature, for instance at  $T_{\text{eq}} = 1000$  K for  $[\text{Fe}/\text{H}] = 2$ . This could be attributed to the middle atmosphere temperature being relatively hotter than that for low-metallicity models, which acts to cause the RCB before the temperature structure converges to the radiative zero solution.

### 3.3. Semi-analytical Model of the Deep Adiabatic

We now derive a semi-analytical fit to the universal thermal structure of deep atmospheres for  $T_{\text{eq}} \sim 250\text{--}1200$  K. Since the deep adiabatic profile would be scaled by the RCB, we infer the parameter dependence of  $P \propto (\kappa_0 g)^{1/(1+\alpha)} T_{\text{int}}^{-4/(1+\alpha)} T^{(4-\beta)/(1+\alpha)}$  from Equation (10). According to Figure 3, the opacity law approximately follows  $\alpha \sim 0.5$  and  $(4-\beta)/(1+\alpha) \sim 4$  in the temperature range of interest. In addition, the reference opacity  $\kappa_0$  depends on the metallicity. We assume the metallicity dependence of  $\kappa_0 \propto 10^{c[\text{Fe}/\text{H}]}$ ,

<sup>3</sup> A Python version of the adopted model has now been made publicly available (Mukherjee et al. 2022a).



where  $c$  is a fitting constant<sup>4</sup>. Inserting these values and determining the reference pressure to match numerical results, we achieve the following analytical form of the deep adiabatic  $P$ - $T$  profile which  $P$ - $T$  profiles converge at  $T_{\text{eq}} \sim 250$ –1200 K, as

$$P \approx 70 \times 10^{-0.4[\text{Fe}/\text{H}]} \text{ bar} \left( \frac{T}{1000 \text{ K}} \right)^4 \left( \frac{g}{10 \text{ m s}^{-2}} \right)^{2/3} \left( \frac{T_{\text{int}}}{100 \text{ K}} \right)^{-8/3}, \quad (15)$$

or equivalently

$$T \approx 1090 \times 10^{0.1[\text{Fe}/\text{H}]} \text{ K} \left( \frac{P}{100 \text{ bar}} \right)^{1/4} \left( \frac{g}{10 \text{ m s}^{-2}} \right)^{-1/6} \left( \frac{T_{\text{int}}}{100 \text{ K}} \right)^{2/3}, \quad (16)$$

where we have inserted  $c \approx 0.6$  to fit the metallicity dependence of the numerical results. Equation (15) indicates that the deep adiabat becomes hotter at higher intrinsic temperature, metallicity, and lower surface gravity. The black dotted lines in Figure 4 show the analytic deep adiabatic  $P$ - $T$  profile of Equation (15). As seen in the Figure, Equation (15) explains the common deep adiabatic profile for  $T_{\text{eq}} \sim 250$ –1200 K very well, including its dependence on surface gravity, intrinsic temperature, and atmospheric metallicity. Thus, for cool to warm exoplanets with  $T_{\text{eq}} \sim 250$ –1200 K, one can utilize Equation (15) to estimate the thermal structure of the deep atmosphere, such as for estimating the quenched abundance of disequilibrium chemical species.

#### 4. EXPLORING THE RELATIONSHIP BETWEEN $\text{NH}_3$ AND BULK NITROGEN ABUNDANCES

In the previous section we worked to derive a semi-analytic theory of the deep atmosphere temperature structure as a step towards a semi-analytic understanding of an atmospheres  $\text{NH}_3$  abundance. We continue along this path here. In this section we explore the relationship between observable  $\text{NH}_3$  and the bulk nitrogen abundance based on semi-analytical arguments.

##### 4.1. Semi-analytical predictions

We first estimate how the vertically quenched  $\text{NH}_3$  abundance relates to the bulk nitrogen abundance based on the semi-analytical argument established in previous sections. Since exoplanets with  $T_{\text{eq}} \sim 250$ –1200 K have nearly the same deep adiabatic profile (Section 3) and  $\text{NH}_3/\text{N}_2$  ratio is nearly constant along the deep adiabat (Section 2.1), the quenched  $\text{NH}_3$  abundance would be nearly independent of the equilibrium temperature, as previously demonstrated in

Fortney et al. (2020). For cool to warm exoplanets with  $T_{\text{eq}} \sim 250$ –1200 K, solving Equation (4) with respect to  $f_{\text{NH}_3}$ , we predict the quenched  $\text{NH}_3$  abundance of

$$\frac{f_{\text{NH}_3}}{f_{\text{N}}} = \frac{\sqrt{1 + 8\mathcal{K}^{-1}} - 1}{4} \mathcal{K}, \quad (17)$$

where

$$\mathcal{K} = P^2 f_{\text{H}_2}^3 f_{\text{N}}^{-1} A e^{B/T} \quad (18)$$

$$\approx 3.46 \times 10^{-0.8[\text{Fe}/\text{H}]} \left( \frac{f_{\text{N}}}{10^{-4}} \right)^{-1} \left( \frac{g}{10 \text{ m s}^{-2}} \right)^{4/3} \left( \frac{T_{\text{int}}}{100 \text{ K}} \right)^{-16/3},$$

where we have inserted the semi-analytic deep adiabat (Equation 15) with  $T = 2000$  K, where the temperature is chosen arbitrary as the equilibrium  $\text{NH}_3$  abundance is approximately constant along the deep adiabat. Qualitatively speaking, low intrinsic temperature, low atmospheric metallicity, and high surface gravity lead to colder deep atmospheres, which corresponds to large  $\mathcal{K}$ . Thus, Equation (17) yields  $\text{NH}_3$  rich deep atmospheres of  $f_{\text{NH}_3} = f_{\text{N}}$  in the limit of high  $\mathcal{K}$  and vice versa for low  $\mathcal{K}$ . Meanwhile, substitution of Equation (15) into (4) with  $T = 2000$  K yields

$$\frac{f_{\text{N}}}{f_{\text{NH}_3}} \approx 1 + 0.58 \times 10^{0.8[\text{Fe}/\text{H}]} \left( \frac{f_{\text{NH}_3}}{10^{-4}} \right) \left( \frac{g}{10 \text{ m s}^{-2}} \right)^{-4/3} \left( \frac{T_{\text{int}}}{100 \text{ K}} \right)^{16/3} \quad (19)$$

Equation (19) enables us to constrain the bulk nitrogen abundance for a given quenched  $\text{NH}_3$  abundance, atmospheric metallicity, surface gravity, and intrinsic temperature. The former three values could be constrained by observations, while the intrinsic temperature could be constrained either by thermal evolution models (e.g., Guillot et al. 1996; Burrows et al. 1997; Guillot & Showman 2002; Baraffe et al. 2003; Fortney et al. 2007; Mordasini et al. 2012; Valencia et al. 2013; Lopez & Fortney 2014; Kurosaki et al. 2014; Kurokawa & Nakamoto 2014; Vazan et al. 2015; Thorngren et al. 2016; Chen & Rogers 2016; Kubyskhina et al. 2020) and/or emission spectroscopy in the limit of very high  $T_{\text{int}}$  (Morley et al. 2017).

Focusing on cool to warm exoplanets, we here predict the quenched  $\text{NH}_3$  abundance and its fraction to the bulk nitrogen,  $f_{\text{NH}_3}/f_{\text{N}}$ , over a wide range of planetary mass and age. We combine Equations (17) and (19) with the thermal evolution tracks of Fortney et al. (2007) to predict  $g$  and  $T_{\text{int}}$  for given planetary masses and ages, where we adopted the evolution track for the core mass of  $10 M_{\oplus}$  and semi-major axis of 0.1 AU<sup>5</sup>. Figure 5 shows the predicted  $\text{NH}_3$  abundance and its fraction of the bulk nitrogen abundance. The quenched  $\text{NH}_3$  abundance is in general higher at lower mass

<sup>4</sup> This dependence is motivated by the analytic Rosseland mean opacity of Freedman et al. (2014), who also assumed the opacity proportional to  $10^{c[\text{Fe}/\text{H}]}$ . Freedman et al. (2014) considered different  $c$  coefficients between high and low pressure limits and also considered a temperature dependence of  $c$  at the high pressure limit. Here, We have assumed a constant value of  $c$  for the sake of simplicity.

<sup>5</sup> Grids of the evolution tracks are available at <https://www.ucolick.org/~jfortney/models.htm>

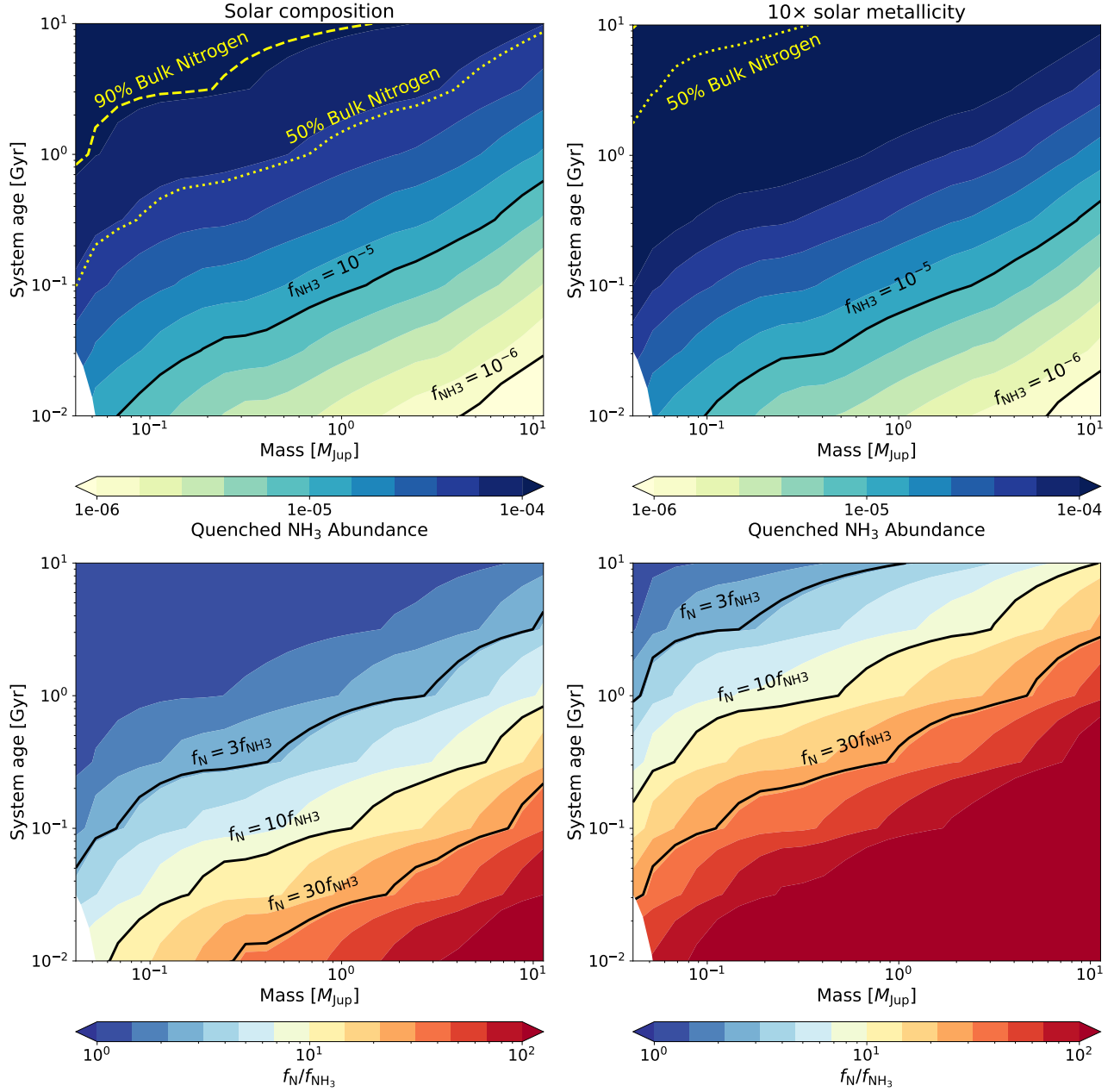


**Figure 5.** The quenched  $\text{NH}_3$  abundance (top panels, Equation 17) and the ratio of the bulk nitrogen to the quenched  $\text{NH}_3$  abundance ratio  $f_{\text{N}}/f_{\text{NH}_3}$  (bottom panels, Equation 19) as a function of a planetary mass and age, applicable to planets that have the universal deep adiabat ( $T_{\text{eq}} \sim 250\text{--}1200$  K). The black line denote the abundance contours of  $f_{\text{NH}_3} = 10^{-5}$  and  $10^{-6}$  for the top panels and the contours of  $f_{\text{N}}/f_{\text{NH}_3} = 3, 10$ , and  $30$  for the bottom panels. The yellow contours in the upper panels also denote the contours of  $\text{NH}_3$  abundances corresponding to the 90% and 50% of bulk nitrogen budget. The left and right columns show the results for solar metallicity and  $10\times$  solar metallicity atmospheres, respectively, where we have assumed that the N/H ratio is scaled by the metallicity.

and older planets, as these planets have cooler interiors and deep atmospheres that allow an  $\text{NH}_3$ -rich deep atmosphere. In many cases, the quenched  $\text{NH}_3$  abundance exceeds what

is a potentially detectable mixing ratio<sup>6</sup> of  $\gtrsim 10^{-6}$  (see Fortney et al. 2020 for the discussion on the threshold), except for super-Jupiter mass planets at very young ages of  $\lesssim 0.01$  Myr.

<sup>6</sup> We note that the actual detectable abundance would depend on a number of other factors, such as wavelength range, spectral resolution, chemical species of interest, and abundances of other chemical species.

In terms of the  $\text{NH}_3$  fraction to the total nitrogen, for solar metallicity atmospheres (left column of Figure 5), the quenched  $\text{NH}_3$  abundance is almost identical to the bulk nitrogen abundance if the planet has a sub-Jupiter mass ( $\lesssim 1 M_J$ ) and old ages ( $\gtrsim 1$  Gyr). For more massive and younger planets, the quenched  $\text{NH}_3$  abundance starts to deviate from the bulk nitrogen abundance. For example, the  $\text{NH}_3$  abundance is approximately an order of magnitude lower than the bulk nitrogen abundance in Jupiter-mass planets at 0.1 Gyr. Thus, for massive and young planets, the observed  $\text{NH}_3$  abundance would only constrain the lower limit of the bulk nitrogen abundance.

The discrepancy between the  $\text{NH}_3$  and bulk nitrogen abundance becomes even larger if the planet has a higher metallicity atmosphere. The right column of Figure 5 shows the quenched  $\text{NH}_3$  abundance and  $f_N/f_{\text{NH}_3}$  for  $10\times$  solar metallicity atmospheres. Interestingly, the expected quenched  $\text{NH}_3$  abundance is almost comparable to that expected for solar metallicity atmospheres, as  $\text{N}_2$  is favored for both higher  $\text{N}/\text{H}$  and hotter deep atmospheres due to higher metallicities. This can also be understood as follows. Assuming a high metallicity atmosphere with  $\mathcal{K} \ll 8$  and  $f_N \propto 10^{[\text{Fe}/\text{H}]}$ , Equation (17) approximately yields the  $\text{NH}_3$  abundance of

$$f_{\text{NH}_3} \approx f_N \sqrt{\frac{\mathcal{K}}{2}} \propto 10^{0.1[\text{Fe}/\text{H}]}. \quad (20)$$

Thus, the  $\text{NH}_3$  abundance is insensitive to  $[\text{Fe}/\text{H}]$  for high metallicity atmospheres. The weak metallicity dependence of  $f_{\text{NH}_3}$  leads to the *fraction* of  $\text{NH}_3$  to the bulk nitrogen, i.e.,  $f_{\text{NH}_3}/f_N$ , being lower in the higher metallicity atmospheres at a given planetary mass and age. In other words, the fraction of observable nitrogen (i.e.,  $\text{NH}_3$ ) decreases with an increased atmospheric metallicity because of the conversion of  $\text{NH}_3$  to  $\text{N}_2$ . Importantly then, it is necessary to assess the overall atmospheric metallicity from other spectral features for correctly inferring the bulk nitrogen abundance from  $\text{NH}_3$ .

## 5. DISCUSSION

### 5.1. Issues of the Strong Dependence on Metallicity

One of our main findings is the strong metallicity dependence of the ratio of the quenched  $\text{NH}_3$  abundance to the bulk nitrogen abundance. Atmospheric metallicity could be constrained by the presence of chemical species sensitive to the metallicity, such as  $\text{CO}_2$  (e.g., *JWST Transiting Exoplanet Community Early Release Science Team et al. 2022; Alderson et al. 2022; Rustamkulov et al. 2022*) and  $\text{SO}_2$  (Polman et al. 2022; Tsai et al. 2022). Broad wavelength coverage and the unprecedented precision of JWST may also help to better constrain the metallicity. Thus, we anticipate that observers can use a planet’s observationally constrained metallicity for converting the retrieved  $\text{NH}_3$  abundance to bulk ni-

trogen abundance through Equation (19). However, the inference would be further complicated if a planetary atmosphere has strongly non-solar elemental ratios (e.g.,  $\text{C}/\text{O} \gg 1$ ), as it may cause a distinct deep adiabatic profile from our semi-analytic  $P$ - $T$  profile.

It is difficult to predict whether the quenched  $\text{NH}_3$  abundance is comparable to the bulk nitrogen abundance before observations. There are a few potential ways to coarsely aid such predictions, however. Interior structure models could set an upper limit on atmospheric metallicity assuming that the metals in the planetary interior is fully mixed to the atmosphere (Thorngren & Fortney 2019). The estimated upper limit may be used to predict the largest discrepancy between the quenched  $\text{NH}_3$  and bulk nitrogen abundance. One might eventually also be able to utilize the relation between planetary mass and atmospheric metallicity suggested from Solar System giant planets (e.g., Kreidberg et al. 2014; Wakeford et al. 2017; Welbanks et al. 2019). However, exoplanets have not shown a clear mass-metallicity relation as of yet (Wakeford & Dalba 2020; Guillot et al. 2022; Edwards et al. 2022). We need better knowledge about the population-level metallicity trend of exoplanetary atmospheres to make a reliable prediction.

### 5.2. Caveats

We have assumed that the  $\text{NH}_3$  abundance is vertically constant above the quench level. While several studies assumed the same approximation to model the transport-driven disequilibrium chemistry (e.g., Morley et al. 2017; Fortney et al. 2020; Mukherjee et al. 2022b), the assumption is not always valid. For example, Moses et al. (2011) showed that  $\text{NH}_3$  abundance gradually decreases with decreasing pressure above the quench level in hot Jupiter HD189733b. Moses et al. (2021) also obtained similar  $\text{NH}_3$  profiles in their pseudo-2D photochemical simulations for many planetary equilibrium temperature. These vertically nonuniform profile could occur when the eddy diffusion timescale is not sufficiently short as compared to chemical interconversion timescale. We anticipate that the vertically constant abundance would be reasonable for warm to cool exoplanets where the chemical timescale quickly increases with altitude (see Tsai et al. 2018). However, one should always be encouraged to verify the assumption using kinetic chemical model for a specific planet of interest.

We have assumed nearly constant equilibrium abundance of  $\text{NH}_3$  along the deep adiabat. While the assumption is reasonably valid at hydrogen-dominated substellar atmospheres, the assumption would be no longer valid if an atmosphere has different a primary composition with different adiabatic index.

We have only considered the transport-induced disequilibrium chemistry, while other physical processes can also affect

the  $\text{NH}_3$  vertical profile. [Molaverdikhani et al. \(2019\)](#) provides an in depth discussion about how the photochemistry and molecular diffusion could cause the discrepancy from vertically constant profile. [Hu \(2021\)](#) showed that  $\text{NH}_3$  tends to be depleted by photodissociation in temperate to cold exoplanets. We investigate the effect of photochemistry and how the observable  $\text{NH}_3$  abundance relates with bulk nitrogen abundance in our Paper II.

### 5.3. Relevance for Cold and Directly Imaged Planets

Planets that lack strong radiative forcing from their parent star would in some ways be simpler to interpret, from an observational perspective. First, lacking external forcing, their interiors would cool off somewhat faster, into the  $\text{NH}_3$  dominated chemical T-P phase space. While their deep atmospheres would not share the radiative-zero solution, they do have the real added benefit that their intrinsic temperature (the object’s effective temperature in this case) and the T-P conditions of their deep atmosphere adiabat can be directly constrained by thermal infrared observations. Moreover, those isolated objects can avoid  $\text{NH}_3$  depletion by photodissociation, which limits the observability of  $\text{NH}_3$  for irradiated planets ([Hu 2021](#)). Nitrogen disequilibrium in the atmospheres of such isolated objects was recently modeled in [Koralidi et al. \(2021\)](#); [Mukherjee et al. \(2022b\)](#).

For the very coldest planets whether irradiated or not, one needs to further consider relevant condensation physics. In cold exoplanets where  $\text{NH}_3$  clouds form,  $\text{NH}_3$  must be depleted above the  $\text{NH}_3$  cloud base, like solar system giant planets. The formation of  $\text{H}_2\text{O}$  clouds may also affect  $\text{NH}_3$  abundances. Recent microwave observations of Jupiter by JUNO revealed that  $\text{NH}_3$  abundance is still partly depleted even below the  $\text{NH}_3$  cloud base ([Bolton et al. 2017](#); [Li et al. 2017](#)). [Guillot et al. \(2020a,b\)](#) suggested that such  $\text{NH}_3$  depletion could be explained by the formation of  $\text{NH}_3\text{-H}_2\text{O}$  condensate.  $\text{NH}_3$  can also be depleted because of the dissolution into liquid  $\text{H}_2\text{O}$  clouds ([Hu 2019](#)). Thus, one needs to be cautious in interpreting the  $\text{NH}_3$  abundances on very cool planets where  $\text{NH}_3$  and/or  $\text{H}_2\text{O}$  clouds potentially form.

## 6. SUMMARY

In this study, we have investigated how observable  $\text{NH}_3$  abundances relate to bulk nitrogen abundances of exoplanetary atmospheres. We first identified that irradiated substellar atmospheres follow nearly the same deep adiabatic profile over a wide range of equilibrium temperatures ( $T_{\text{eq}} \sim 250\text{--}1200$  K). We have derived a semi-analytical model of such a universal deep adiabat (Equation 15) that readily explains the radiative-convective equilibrium model. Then, we established a semi-analytical model that relates vertically quenched  $\text{NH}_3$  abundances with the bulk nitrogen abundance of the atmosphere (Equation 19). Based on the

semi-analytical model, we predict the relation between the quenched  $\text{NH}_3$  and bulk nitrogen abundances as a function of planetary mass and age. We verify our semi-analytical model using a photochemical kinetic model in Paper II. Our key findings are summarized as follows:

1. Irradiated giant planet atmospheres have nearly the same deep adiabatic profile for the equilibrium temperature of  $T_{\text{eq}} \sim 250\text{--}1200$  K for a given set of planetary gravity and intrinsic temperature. This is caused by the fact that their atmospheric  $P\text{--}T$  profiles tend to converge to the radiative-zero solution that is independent of the upper boundary conditions before they meet the radiative convective boundary (Section 3). Based on the series of radiative-convective equilibrium calculations, we have derived a semi-analytical model of such universal deep adiabats applicable to planets with  $T_{\text{eq}} \sim 250\text{--}1200$  K (Section 3.2, Equations 15 or 16).
2. We have established a semi-analytical model that relates the vertically quenched  $\text{NH}_3$  abundance with the bulk nitrogen abundance (Equations 17 and 19). Our model is applicable to warm irradiated giant exoplanets. We are able to readily assess discrepancies between the quenched  $\text{NH}_3$  and bulk nitrogen abundances. This aids when attempting to infer the bulk nitrogen abundance from an observed  $\text{NH}_3$  abundance.
3. At solar composition in a giant planet atmosphere, the vertically quenched  $\text{NH}_3$  abundance nearly coincides with the bulk nitrogen abundance *only* when a planet has a sub-Jupiter mass ( $\lesssim 1 M_J$ ) and old age ( $\gtrsim 1$  Gyr). For planets with super-Jupiter mass and/or age younger than 1 Gyr, in contrast, the quenched  $\text{NH}_3$  abundance is considerably lower than the bulk nitrogen abundance, as the deep atmosphere is so hot that  $\text{N}_2$  dominates over  $\text{NH}_3$ . (Section 4 and Figure 5).
4. As the atmospheric metallicity increases, while the predicted quenched  $\text{NH}_3$  mixing ratio remains constant at a given mass and age, the ratio of  $\text{NH}_3$  to the bulk atmospheric nitrogen abundance decreases significantly. The issue of  $\text{NH}_3$  only containing a fraction of the bulk nitrogen abundance then occurs across all giant planet phase space, at sub-Jupiter planet masses and old ages. This “missing nitrogen” problem can be corrected with an assessment of the deep atmospheric T-P profile (likely from structure or evolution models) and an overall assessment of atmospheric metallicity from other species, such as C- and O-bearing molecules, or alkali metals.

## ACKNOWLEDGEMENTS



We are grateful to anonymous reviewer for their insightful comments that greatly improved the quality of this paper. We thank Masahiro Ikoma for helpful comments on the thermal structures of deep atmospheres. We also thank Neel Patel, Xinting Yu, Ben Lew, Eliza Kempton, Yuichi Ito, Yui Kawashima, Shota Notsu, Tatsuya Yoshida, and Akifumi Nakayama for fruitful discussions. This work benefited from the 2022 Exoplanet Summer Program in the Other

Worlds Laboratory (OWL) at the University of California, Santa Cruz, a program funded by the Heising-Simons Foundation. Most of numerical computations were carried out on PC cluster at Center for Computational Astrophysics, National Astronomical Observatory of Japan. K.O. was supported by JSPS Overseas Research Fellowship. J.J.F. is supported by an award from the Simons Foundation.

## APPENDIX

### 1. PHYSICAL MEANING OF $\phi$ PARAMETER

In this appendix, we elaborate on the physical meaning of  $\phi$ , which is introduced in Section 3 to quantify whether the  $P$ – $T$  profile converges to the radiative-zero solution above the RCB pressure level. The radiative temperature gradient (Equation 5) approaches zero in the limit of  $P \rightarrow 0$  and increases with increasing the pressure. However, the gradient does not increase indefinitely. It converges to a certain value controlled by the opacity law. Inserting back the radiative-zero solution (Equation 6 with  $T_0 = 0$  and  $P_0 = 0$ ) into (5), one can find an asymptotic gradient to which the radiative gradient approaches:

$$\left(\frac{d \ln T}{d \ln P}\right)_{\text{rad,limit}} = \frac{1 + \alpha}{4 - \beta}. \quad (1)$$

Thus, the definition of  $\phi$  parameter (Equation 12) can be understood as the ratio of the adiabatic gradient  $\nabla_{\text{ad}}$  to the above asymptotic radiative gradient:

$$\phi \equiv \frac{4 - \beta}{1 + \alpha} \nabla_{\text{ad}} = \frac{(d \ln T / d \ln P)_{\text{ad}}}{(d \ln T / d \ln P)_{\text{rad,limit}}}. \quad (2)$$

If the asymptotic radiative gradient is much larger than the adiabatic gradient, i.e.,  $\phi \ll 1$ , convection would quickly set in before the  $P$ – $T$  profile converges to the radiative-zero solution with the asymptotic gradient. By contrast,  $\phi > 1$  means that the radiative gradient never exceeds the adiabatic gradient even in the limit of deep atmospheres. Thus, convection does not occur for  $\phi > 1$ .

## REFERENCES

- Alderson, L., Wakeford, H. R., Alam, M. K., et al. 2022, arXiv e-prints, arXiv:2211.10488. <https://arxiv.org/abs/2211.10488>
- Ali-Dib, M., Mousis, O., Petit, J.-M., & Lunine, J. I. 2014, *ApJ*, 785, 125, doi: [10.1088/0004-637X/785/2/125](https://doi.org/10.1088/0004-637X/785/2/125)
- Asplund, M., Amarsi, A. M., & Grevesse, N. 2021, *A&A*, 653, A141, doi: [10.1051/0004-6361/202140445](https://doi.org/10.1051/0004-6361/202140445)
- Atreya, S. K., Crida, A., Guillot, T., et al. 2022, arXiv e-prints, arXiv:2205.06914. <https://arxiv.org/abs/2205.06914>
- Baraffe, I., Chabrier, G., Barman, T. S., Allard, F., & Hauschildt, P. H. 2003, *A&A*, 402, 701, doi: [10.1051/0004-6361:20030252](https://doi.org/10.1051/0004-6361:20030252)
- Bitsch, B., Schneider, A. D., & Kreidberg, L. 2022, arXiv e-prints, arXiv:2207.06077. <https://arxiv.org/abs/2207.06077>
- Bolton, S. J., Adriani, A., Adumitroaie, V., et al. 2017, *Science*, 356, 821, doi: [10.1126/science.aal2108](https://doi.org/10.1126/science.aal2108)
- Booth, R. A., Clarke, C. J., Madhusudhan, N., & Ilee, J. D. 2017, *MNRAS*, 469, 3994, doi: [10.1093/mnras/stx1103](https://doi.org/10.1093/mnras/stx1103)
- Booth, R. A., & Ilee, J. D. 2019, *MNRAS*, 487, 3998, doi: [10.1093/mnras/stz1488](https://doi.org/10.1093/mnras/stz1488)
- Bosman, A. D., Cridland, A. J., & Miguel, Y. 2019, *A&A*, 632, L11, doi: [10.1051/0004-6361/201936827](https://doi.org/10.1051/0004-6361/201936827)
- Burrows, A., Marley, M., Hubbard, W. B., et al. 1997, *ApJ*, 491, 856, doi: [10.1086/305002](https://doi.org/10.1086/305002)
- Chabrier, G., Mazevet, S., & Soubiran, F. 2019, *ApJ*, 872, 51, doi: [10.3847/1538-4357/aaf99f](https://doi.org/10.3847/1538-4357/aaf99f)
- Chachan, Y., Knutson, H. A., Lothringer, J., & Blake, G. A. 2022, arXiv e-prints, arXiv:2211.09080. <https://arxiv.org/abs/2211.09080>
- Chen, H., & Rogers, L. A. 2016, *ApJ*, 831, 180, doi: [10.3847/0004-637X/831/2/180](https://doi.org/10.3847/0004-637X/831/2/180)
- Cridland, A. J., Pudritz, R. E., & Alessi, M. 2016, *MNRAS*, 461, 3274, doi: [10.1093/mnras/stw1511](https://doi.org/10.1093/mnras/stw1511)
- Cridland, A. J., Pudritz, R. E., Birnstiel, T., Cleves, L. I., & Bergin, E. A. 2017, *MNRAS*, 469, 3910, doi: [10.1093/mnras/stx1069](https://doi.org/10.1093/mnras/stx1069)
- Cridland, A. J., van Dishoeck, E. F., Alessi, M., & Pudritz, R. E. 2019, *A&A*, 632, A63, doi: [10.1051/0004-6361/201936105](https://doi.org/10.1051/0004-6361/201936105)

- . 2020, *A&A*, 642, A229, doi: [10.1051/0004-6361/202038767](https://doi.org/10.1051/0004-6361/202038767)
- Dash, S., Majumdar, L., Willacy, K., et al. 2022, arXiv e-prints, arXiv:2204.04103. <https://arxiv.org/abs/2204.04103>
- Drummond, B., Carter, A. L., Hébrard, E., et al. 2019, *MNRAS*, 486, 1123, doi: [10.1093/mnras/stz909](https://doi.org/10.1093/mnras/stz909)
- Edwards, B., Changeat, Q., Tsiaras, A., et al. 2022, arXiv e-prints, arXiv:2211.00649. <https://arxiv.org/abs/2211.00649>
- Eistrup, C. 2022, arXiv e-prints, arXiv:2210.16921. <https://arxiv.org/abs/2210.16921>
- Eistrup, C., Cleves, L. I., & Krijt, S. 2022, arXiv e-prints, arXiv:2207.13158. <https://arxiv.org/abs/2207.13158>
- Eistrup, C., Walsh, C., & van Dishoeck, E. F. 2016, *A&A*, 595, A83, doi: [10.1051/0004-6361/201628509](https://doi.org/10.1051/0004-6361/201628509)
- . 2018, *A&A*, 613, A14, doi: [10.1051/0004-6361/201731302](https://doi.org/10.1051/0004-6361/201731302)
- Espinoza, N., Fortney, J. J., Miguel, Y., Thorngren, D., & Murray-Clay, R. 2017, *ApJL*, 838, L9, doi: [10.3847/2041-8213/aa65ca](https://doi.org/10.3847/2041-8213/aa65ca)
- Fegley, B., J., & Prinn, R. G. 1985, *ApJ*, 299, 1067, doi: [10.1086/163775](https://doi.org/10.1086/163775)
- Fegley, Bruce, J., & Lodders, K. 1994, *Icarus*, 110, 117, doi: [10.1006/icar.1994.1111](https://doi.org/10.1006/icar.1994.1111)
- Fortney, J. J., Ikoma, M., Nettelmann, N., Guillot, T., & Marley, M. S. 2011, *ApJ*, 729, 32, doi: [10.1088/0004-637X/729/1/32](https://doi.org/10.1088/0004-637X/729/1/32)
- Fortney, J. J., Lodders, K., Marley, M. S., & Freedman, R. S. 2008, *ApJ*, 678, 1419, doi: [10.1086/528370](https://doi.org/10.1086/528370)
- Fortney, J. J., Marley, M. S., & Barnes, J. W. 2007, *ApJ*, 659, 1661, doi: [10.1086/512120](https://doi.org/10.1086/512120)
- Fortney, J. J., Marley, M. S., Lodders, K., Saumon, D., & Freedman, R. 2005, *ApJL*, 627, L69, doi: [10.1086/431952](https://doi.org/10.1086/431952)
- Fortney, J. J., Visscher, C., Marley, M. S., et al. 2020, *AJ*, 160, 288, doi: [10.3847/1538-3881/abc5bd](https://doi.org/10.3847/1538-3881/abc5bd)
- Freedman, R. S., Lustig-Yaeger, J., Fortney, J. J., et al. 2014, *ApJS*, 214, 25, doi: [10.1088/0067-0049/214/2/25](https://doi.org/10.1088/0067-0049/214/2/25)
- Gao, P., Thorngren, D. P., Lee, G. K. H., et al. 2020, *Nature Astronomy*, doi: [10.1038/s41550-020-1114-3](https://doi.org/10.1038/s41550-020-1114-3)
- Ginzburg, S., Schlichting, H. E., & Sari, R. 2018, *MNRAS*, 476, 759, doi: [10.1093/mnras/sty290](https://doi.org/10.1093/mnras/sty290)
- Guillot, T. 2010, *A&A*, 520, A27, doi: [10.1051/0004-6361/200913396](https://doi.org/10.1051/0004-6361/200913396)
- Guillot, T., Burrows, A., Hubbard, W. B., Lunine, J. I., & Saumon, D. 1996, *ApJL*, 459, L35, doi: [10.1086/309935](https://doi.org/10.1086/309935)
- Guillot, T., Fletcher, L. N., Helled, R., et al. 2022, arXiv e-prints, arXiv:2205.04100. <https://arxiv.org/abs/2205.04100>
- Guillot, T., & Showman, A. P. 2002, *A&A*, 385, 156, doi: [10.1051/0004-6361:20011624](https://doi.org/10.1051/0004-6361:20011624)
- Guillot, T., Stevenson, D. J., Atreya, S. K., Bolton, S. J., & Becker, H. N. 2020a, *Journal of Geophysical Research (Planets)*, 125, e06403, doi: [10.1029/2020JE006403](https://doi.org/10.1029/2020JE006403)
- Guillot, T., Li, C., Bolton, S. J., et al. 2020b, *Journal of Geophysical Research (Planets)*, 125, e06404, doi: [10.1029/2020JE006404](https://doi.org/10.1029/2020JE006404)
- Hands, T. O., & Helled, R. 2022, *MNRAS*, 509, 894, doi: [10.1093/mnras/stab2967](https://doi.org/10.1093/mnras/stab2967)
- Hayashi, C., Hōshi, R., & Sugimoto, D. 1962, *Progress of Theoretical Physics Supplement*, 22, 1, doi: [10.1143/PTPS.22.1](https://doi.org/10.1143/PTPS.22.1)
- Helling, C., Woitke, P., Rimmer, P. B., et al. 2014, *Life*, 4, 142, doi: [10.3390/life4020142](https://doi.org/10.3390/life4020142)
- Hobbs, R., Shorttle, O., Madhusudhan, N., & Rimmer, P. 2019, *MNRAS*, 487, 2242, doi: [10.1093/mnras/stz1333](https://doi.org/10.1093/mnras/stz1333)
- Hu, R. 2019, *ApJ*, 887, 166, doi: [10.3847/1538-4357/ab58c7](https://doi.org/10.3847/1538-4357/ab58c7)
- . 2021, *ApJ*, 921, 27, doi: [10.3847/1538-4357/ac1789](https://doi.org/10.3847/1538-4357/ac1789)
- JWST Transiting Exoplanet Community Early Release Science Team, Ahrer, E.-M., Alderson, L., Batalha, N. M., et al. 2022, *Nature*
- Karalidi, T., Marley, M., Fortney, J. J., et al. 2021, *ApJ*, 923, 269, doi: [10.3847/1538-4357/ac3140](https://doi.org/10.3847/1538-4357/ac3140)
- Kawashima, Y., & Min, M. 2021, *A&A*, 656, A90, doi: [10.1051/0004-6361/202141548](https://doi.org/10.1051/0004-6361/202141548)
- Kippenhahn, R., & Weigert, A. 1994, *Stellar Structure and Evolution*
- Kreidberg, L., Bean, J. L., Désert, J.-M., et al. 2014, *ApJL*, 793, L27, doi: [10.1088/2041-8205/793/2/L27](https://doi.org/10.1088/2041-8205/793/2/L27)
- Kubyskhina, D., Vidotto, A. A., Fossati, L., & Farrell, E. 2020, *MNRAS*, 499, 77, doi: [10.1093/mnras/staa2815](https://doi.org/10.1093/mnras/staa2815)
- Kurokawa, H., & Nakamoto, T. 2014, *ApJ*, 783, 54, doi: [10.1088/0004-637X/783/1/54](https://doi.org/10.1088/0004-637X/783/1/54)
- Kurosaki, K., Ikoma, M., & Hori, Y. 2014, *A&A*, 562, A80, doi: [10.1051/0004-6361/201322258](https://doi.org/10.1051/0004-6361/201322258)
- Li, C., Ingersoll, A., Janssen, M., et al. 2017, *Geophys. Res. Lett.*, 44, 5317, doi: [10.1002/2017GL073159](https://doi.org/10.1002/2017GL073159)
- Line, M. R., Vasisht, G., Chen, P., Angerhausen, D., & Yung, Y. L. 2011, *ApJ*, 738, 32, doi: [10.1088/0004-637X/738/1/32](https://doi.org/10.1088/0004-637X/738/1/32)
- Lodders, K., & Fegley, B. 2002, *Icarus*, 155, 393, doi: [10.1006/icar.2001.6740](https://doi.org/10.1006/icar.2001.6740)
- Lopez, E. D., & Fortney, J. J. 2014, *ApJ*, 792, 1, doi: [10.1088/0004-637X/792/1/1](https://doi.org/10.1088/0004-637X/792/1/1)
- Lothringer, J. D., Rustamkulov, Z., Sing, D. K., et al. 2021, *ApJ*, 914, 12, doi: [10.3847/1538-4357/abf8a9](https://doi.org/10.3847/1538-4357/abf8a9)
- Lupu, R., Freedman, R., & Visscher, C. 2021, Correlated k coefficients for H<sub>2</sub>-He atmospheres; 196 spectral windows and 1060 pressure-temperature points, Zenodo, doi: [10.5281/zenodo.6708165](https://doi.org/10.5281/zenodo.6708165)
- MacDonald, R. J., & Madhusudhan, N. 2017, *ApJL*, 850, L15, doi: [10.3847/2041-8213/aa97d4](https://doi.org/10.3847/2041-8213/aa97d4)
- Madhusudhan, N. 2012, *ApJ*, 758, 36, doi: [10.1088/0004-637X/758/1/36](https://doi.org/10.1088/0004-637X/758/1/36)
- Madhusudhan, N., Amin, M. A., & Kennedy, G. M. 2014, *ApJL*, 794, L12, doi: [10.1088/2041-8205/794/1/L12](https://doi.org/10.1088/2041-8205/794/1/L12)

- Madhusudhan, N., Bitsch, B., Johansen, A., & Eriksson, L. 2017, *MNRAS*, 469, 4102, doi: [10.1093/mnras/stx1139](https://doi.org/10.1093/mnras/stx1139)
- Marley, M. S., & McKay, C. P. 1999, *Icarus*, 138, 268, doi: [10.1006/icar.1998.6071](https://doi.org/10.1006/icar.1998.6071)
- Marley, M. S., & Robinson, T. D. 2015, *ARA&A*, 53, 279, doi: [10.1146/annurev-astro-082214-122522](https://doi.org/10.1146/annurev-astro-082214-122522)
- Marley, M. S., Saumon, D., Guillot, T., et al. 1996, *Science*, 272, 1919, doi: [10.1126/science.272.5270.1919](https://doi.org/10.1126/science.272.5270.1919)
- Marley, M. S., Saumon, D., Visscher, C., et al. 2021, *ApJ*, 920, 85, doi: [10.3847/1538-4357/ac141d](https://doi.org/10.3847/1538-4357/ac141d)
- Mayorga, L. C., Robinson, T. D., Marley, M. S., May, E. M., & Stevenson, K. B. 2021, *ApJ*, 915, 41, doi: [10.3847/1538-4357/abff50](https://doi.org/10.3847/1538-4357/abff50)
- McKay, C. P., Pollack, J. B., & Courtin, R. 1989, *Icarus*, 80, 23, doi: [10.1016/0019-1035\(89\)90160-7](https://doi.org/10.1016/0019-1035(89)90160-7)
- Miles, B. E., Skemer, A. J. I., Morley, C. V., et al. 2020, *AJ*, 160, 63, doi: [10.3847/1538-3881/ab9114](https://doi.org/10.3847/1538-3881/ab9114)
- Mizuno, H. 1980, *Progress of Theoretical Physics*, 64, 544, doi: [10.1143/PTP.64.544](https://doi.org/10.1143/PTP.64.544)
- Molaverdikhani, K., Henning, T., & Mollière, P. 2019, *ApJ*, 883, 194, doi: [10.3847/1538-4357/ab3e30](https://doi.org/10.3847/1538-4357/ab3e30)
- Mollière, P., van Boekel, R., Dullemond, C., Henning, T., & Mordasini, C. 2015, *ApJ*, 813, 47, doi: [10.1088/0004-637X/813/1/47](https://doi.org/10.1088/0004-637X/813/1/47)
- Mollière, P., Molyarova, T., Bitsch, B., et al. 2022, arXiv e-prints, arXiv:2204.13714. <https://arxiv.org/abs/2204.13714>
- Mordasini, C., Alibert, Y., Klahr, H., & Henning, T. 2012, *A&A*, 547, A111, doi: [10.1051/0004-6361/201118457](https://doi.org/10.1051/0004-6361/201118457)
- Morley, C. V., Fortney, J. J., Kempton, E. M.-R., et al. 2013, *ApJ*, 775, 33, doi: [10.1088/0004-637X/775/1/33](https://doi.org/10.1088/0004-637X/775/1/33)
- Morley, C. V., Fortney, J. J., Marley, M. S., et al. 2012, *ApJ*, 756, 172, doi: [10.1088/0004-637X/756/2/172](https://doi.org/10.1088/0004-637X/756/2/172)
- . 2015, *ApJ*, 815, 110, doi: [10.1088/0004-637X/815/2/110](https://doi.org/10.1088/0004-637X/815/2/110)
- Morley, C. V., Knutson, H., Line, M., et al. 2017, *AJ*, 153, 86, doi: [10.3847/1538-3881/153/2/86](https://doi.org/10.3847/1538-3881/153/2/86)
- Morley, C. V., Marley, M. S., Fortney, J. J., et al. 2014, *ApJ*, 787, 78, doi: [10.1088/0004-637X/787/1/78](https://doi.org/10.1088/0004-637X/787/1/78)
- Moses, J. I., Madhusudhan, N., Visscher, C., & Freedman, R. S. 2013a, *ApJ*, 763, 25, doi: [10.1088/0004-637X/763/1/25](https://doi.org/10.1088/0004-637X/763/1/25)
- Moses, J. I., Tremblin, P., Venot, O., & Miguel, Y. 2021, *Experimental Astronomy*, doi: [10.1007/s10686-021-09749-1](https://doi.org/10.1007/s10686-021-09749-1)
- Moses, J. I., Visscher, C., Fortney, J. J., et al. 2011, *ApJ*, 737, 15, doi: [10.1088/0004-637X/737/1/15](https://doi.org/10.1088/0004-637X/737/1/15)
- Moses, J. I., Line, M. R., Visscher, C., et al. 2013b, *ApJ*, 777, 34, doi: [10.1088/0004-637X/777/1/34](https://doi.org/10.1088/0004-637X/777/1/34)
- Mukherjee, S., Batalha, N. E., Fortney, J. J., & Marley, M. S. 2022a, arXiv e-prints, arXiv:2208.07836. <https://arxiv.org/abs/2208.07836>
- Mukherjee, S., Fortney, J. J., Batalha, N. E., et al. 2022b, arXiv e-prints, arXiv:2208.14317. <https://arxiv.org/abs/2208.14317>
- Notsu, S., Eistrup, C., Walsh, C., & Nomura, H. 2020, *MNRAS*, 499, 2229, doi: [10.1093/mnras/staa2944](https://doi.org/10.1093/mnras/staa2944)
- Notsu, S., Ohno, K., Ueda, T., et al. 2022, *ApJ*, 936, 188, doi: [10.3847/1538-4357/ac87fa](https://doi.org/10.3847/1538-4357/ac87fa)
- Öberg, K. I., & Bergin, E. A. 2016, *ApJL*, 831, L19, doi: [10.3847/2041-8205/831/2/L19](https://doi.org/10.3847/2041-8205/831/2/L19)
- . 2021, *PhR*, 893, 1, doi: [10.1016/j.physrep.2020.09.004](https://doi.org/10.1016/j.physrep.2020.09.004)
- Öberg, K. I., Murray-Clay, R., & Bergin, E. A. 2011, *ApJL*, 743, L16, doi: [10.1088/2041-8205/743/1/L16](https://doi.org/10.1088/2041-8205/743/1/L16)
- Öberg, K. I., & Wordsworth, R. 2019, *AJ*, 158, 194, doi: [10.3847/1538-3881/ab46a8](https://doi.org/10.3847/1538-3881/ab46a8)
- Ohno, K., & Fortney, J. 2022
- Ohno, K., & Ueda, T. 2021, *A&A*, 651, L2, doi: [10.1051/0004-6361/202141169](https://doi.org/10.1051/0004-6361/202141169)
- Owen, J. E., & Wu, Y. 2017, *ApJ*, 847, 29, doi: [10.3847/1538-4357/aa890a](https://doi.org/10.3847/1538-4357/aa890a)
- Owen, T., Mahaffy, P., Niemann, H. B., et al. 1999, *Nature*, 402, 269, doi: [10.1038/46232](https://doi.org/10.1038/46232)
- Pacetti, E., Turrini, D., Schisano, E., et al. 2022, arXiv e-prints, arXiv:2206.14685. <https://arxiv.org/abs/2206.14685>
- Piso, A.-M. A., Öberg, K. I., Birnstiel, T., & Murray-Clay, R. A. 2015, *ApJ*, 815, 109, doi: [10.1088/0004-637X/815/2/109](https://doi.org/10.1088/0004-637X/815/2/109)
- Piso, A.-M. A., Pegues, J., & Öberg, K. I. 2016, *ApJ*, 833, 203, doi: [10.3847/1538-4357/833/2/203](https://doi.org/10.3847/1538-4357/833/2/203)
- Polman, J., Waters, L. B. F. M., Min, M., Miguel, Y., & Khorshid, N. 2022, arXiv e-prints, arXiv:2208.00469. <https://arxiv.org/abs/2208.00469>
- Prinn, R. G., & Barshay, S. S. 1977, *Science*, 198, 1031, doi: [10.1126/science.198.4321.1031](https://doi.org/10.1126/science.198.4321.1031)
- Ramírez, V., Cridland, A. J., & Mollière, P. 2020, *A&A*, 641, A87, doi: [10.1051/0004-6361/202038186](https://doi.org/10.1051/0004-6361/202038186)
- Robinson, T. D., & Marley, M. S. 2014, *ApJ*, 785, 158, doi: [10.1088/0004-637X/785/2/158](https://doi.org/10.1088/0004-637X/785/2/158)
- Rogers, L. A., & Seager, S. 2010, *ApJ*, 712, 974, doi: [10.1088/0004-637X/712/2/974](https://doi.org/10.1088/0004-637X/712/2/974)
- Rustamkulov, Z., Sing, D. K., Mukherjee, S., et al. 2022, arXiv e-prints, arXiv:2211.10487. <https://arxiv.org/abs/2211.10487>
- Saumon, D., Chabrier, G., & van Horn, H. M. 1995, *ApJS*, 99, 713, doi: [10.1086/192204](https://doi.org/10.1086/192204)
- Saumon, D., & Marley, M. S. 2008, *ApJ*, 689, 1327, doi: [10.1086/592734](https://doi.org/10.1086/592734)
- Saumon, D., Marley, M. S., Cushing, M. C., et al. 2006, *ApJ*, 647, 552, doi: [10.1086/505419](https://doi.org/10.1086/505419)
- Schneider, A. D., & Bitsch, B. 2021a, *A&A*, 654, A71, doi: [10.1051/0004-6361/202039640](https://doi.org/10.1051/0004-6361/202039640)
- . 2021b, *A&A*, 654, A72, doi: [10.1051/0004-6361/202141096](https://doi.org/10.1051/0004-6361/202141096)
- Stevenson, D. J. 1982, *Planet. Space Sci.*, 30, 755, doi: [10.1016/0032-0633\(82\)90108-8](https://doi.org/10.1016/0032-0633(82)90108-8)
- Tang, S.-Y., Robinson, T. D., Marley, M. S., et al. 2021, *ApJ*, 922, 26, doi: [10.3847/1538-4357/ac1e90](https://doi.org/10.3847/1538-4357/ac1e90)

- Thiabaud, A., Marboeuf, U., Alibert, Y., Leya, I., & Mezger, K. 2015, *A&A*, 574, A138, doi: [10.1051/0004-6361/201424868](https://doi.org/10.1051/0004-6361/201424868)
- Thorngren, D., & Fortney, J. J. 2019, *ApJL*, 874, L31, doi: [10.3847/2041-8213/ab1137](https://doi.org/10.3847/2041-8213/ab1137)
- Thorngren, D., Gao, P., & Fortney, J. J. 2019, *ApJL*, 884, L6, doi: [10.3847/2041-8213/ab43d0](https://doi.org/10.3847/2041-8213/ab43d0)
- Thorngren, D. P., Fortney, J. J., Murray-Clay, R. A., & Lopez, E. D. 2016, *ApJ*, 831, 64, doi: [10.3847/0004-637X/831/1/64](https://doi.org/10.3847/0004-637X/831/1/64)
- Toon, O. B., McKay, C. P., Ackerman, T. P., & Santhanam, K. 1989, *J. Geophys. Res.*, 94, 16287, doi: [10.1029/JD094iD13p16287](https://doi.org/10.1029/JD094iD13p16287)
- Tsai, S.-M., Kitzmann, D., Lyons, J. R., et al. 2018, *ApJ*, 862, 31, doi: [10.3847/1538-4357/aac834](https://doi.org/10.3847/1538-4357/aac834)
- Tsai, S.-M., Lyons, J. R., Grosheintz, L., et al. 2017, *ApJS*, 228, 20, doi: [10.3847/1538-4365/228/2/20](https://doi.org/10.3847/1538-4365/228/2/20)
- Tsai, S.-M., Malik, M., Kitzmann, D., et al. 2021, *ApJ*, 923, 264, doi: [10.3847/1538-4357/ac29bc](https://doi.org/10.3847/1538-4357/ac29bc)
- Tsai, S.-M., Lee, E. K. H., Powell, D., et al. 2022, arXiv e-prints, arXiv:2211.10490. <https://arxiv.org/abs/2211.10490>
- Turrini, D., Schisano, E., Fonte, S., et al. 2021, *ApJ*, 909, 40, doi: [10.3847/1538-4357/abd6e5](https://doi.org/10.3847/1538-4357/abd6e5)
- Valencia, D., Guillot, T., Parmentier, V., & Freedman, R. S. 2013, *ApJ*, 775, 10, doi: [10.1088/0004-637X/775/1/10](https://doi.org/10.1088/0004-637X/775/1/10)
- Vazan, A., Helled, R., Kovetz, A., & Podolak, M. 2015, *ApJ*, 803, 32, doi: [10.1088/0004-637X/803/1/32](https://doi.org/10.1088/0004-637X/803/1/32)
- Venot, O., Hébrard, E., Agúndez, M., et al. 2013, in *Astrophysics and Space Science Proceedings*, Vol. 35, The Early Evolution of the Atmospheres of Terrestrial Planets, ed. J. M. Trigo-Rodríguez, F. Raulin, C. Muller, & C. Nixon, 67, doi: [K18-74538](https://doi.org/10.1007/978-94-007-7453-8_4)
- Visscher, C., Lodders, K., & Fegley, Bruce, J. 2006, *ApJ*, 648, 1181, doi: [10.1086/506245](https://doi.org/10.1086/506245)
- . 2010, *ApJ*, 716, 1060, doi: [10.1088/0004-637X/716/2/1060](https://doi.org/10.1088/0004-637X/716/2/1060)
- Wakeford, H. R., & Dalba, P. A. 2020, *Philosophical Transactions of the Royal Society of London Series A*, 378, 20200054, doi: [10.1098/rsta.2020.0054](https://doi.org/10.1098/rsta.2020.0054)
- Wakeford, H. R., Sing, D. K., Kataria, T., et al. 2017, *Science*, 356, 628, doi: [10.1126/science.aah4668](https://doi.org/10.1126/science.aah4668)
- Welbanks, L., Madhusudhan, N., Allard, N. F., et al. 2019, *ApJL*, 887, L20, doi: [10.3847/2041-8213/ab5a89](https://doi.org/10.3847/2041-8213/ab5a89)
- Zahnle, K. J., & Marley, M. S. 2014, *ApJ*, 797, 41, doi: [10.1088/0004-637X/797/1/41](https://doi.org/10.1088/0004-637X/797/1/41)